Tuning bubbly structures in microchannels

Sharon M. Vuong[1] and Shelley L. Anna[1,2,a]

[1]*Department of Chemical Engineering, Carnegie Mellon University, Pittsburgh, Pennsylvania 15213, USA*
[2]*Department of Mechanical Engineering, Carnegie Mellon University, Pittsburgh, Pennsylvania 15213, USA*

Foams have many useful applications that arise from the structure and size distribution of the bubbles within them. Microfluidics allows for the rapid formation of uniform bubbles, where bubble size and volume fraction are functions of the input gas pressure, liquid flow rate, and device geometry. After formation, the microchannel confines the bubbles and determines the resulting foam structure. Bubbly structures can vary from a single row ("dripping"), to multiple rows ("alternating"), to densely packed bubbles ("bamboo" and dry foams). We show that each configuration arises in a distinct region of the operating space defined by bubble volume and volume fraction. We describe the boundaries between these regions using geometric arguments and show that the boundaries are functions of the channel aspect ratio. We compare these geometric arguments with foam structures observed in experiments using flow-focusing, T-junction, and co-flow designs to generate stable nitrogen bubbles in aqueous surfactant solution and stable droplets in oil containing dissolved surfactant. The outcome of this work is a set of design parameters that can be used to achieve desired foam structures as a function of device geometry and experimental control parameters. © *2012 American Institute of Physics*. [http://dx.doi.org/10.1063/1.3693605]

I. INTRODUCTION

Bubbles and droplets form the basic constituents of foams and emulsions, which have interesting bulk properties arising from the bubble size, size distribution, and placement within the surrounding medium. Foam or emulsion structure is particularly important in a number of applications. A regular spatial structure of monodisperse pores provides a 3D model tissue scaffold system that mimics the extracellular matrix and can be used to perform systematic studies of intercellular mechanisms.[1] The sound frequencies that can be transmitted through a bubbly medium depend on the spacing, crystal structure, and size of the bubbles within that medium.[2] In lab-on-a-chip devices, the packing of monodisperse drop reactors into ordered arrays enables high throughput assays.[3]

In microscale geometries, the minimal impact of inertia and the strong influence of viscous stresses and capillarity lead to regular breakup of the dispersed phase stream to form monodisperse bubbles and droplets.[4–7] The resulting bubble or droplet volume and the qualitative foam or emulsion structure have been shown to be functions of fluid properties, operating flow parameters, and channel geometry.[1,4,5,7–10] The presence of surface active species such as surfactants, proteins, and nanoparticles will also influence the dispersed phase size, shape, and structure.[6,9,11] Scaling arguments and simplified models using the capillary number Ca and the volumetric flow rate ratio have been developed to characterize bubble and droplet size and frequency of formation, but relatively little attention has been given to describing the downstream shape and structure of bubbles or droplets within a given device.[5,6,12]

---

[a]Author to whom correspondence should be addressed. Electronic mail: sanna@cmu.edu.

The structure of a foam is determined by the bubble volume and the gas volume fraction in the foam and is strongly influenced by the presence of physical boundaries.[13] In general, dry foams are those with high gas fractions and faceted bubbles that form Plateau borders with neighboring bubbles.[13] In contrast, wet foams contain larger liquid fractions such that the bubbles maintain a more spherical shape.[7,14] When a foam is contained within a duct of comparable dimensions to the bubble size, the channel geometry influences bubble shape and arrangement. For example, in a rectangular microchannel, if the bubble size increases for a fixed gas fraction, the bubbles will become too large to fit within the rectangular channel cross-section as a sphere. When the bubble diameter exceeds the channel depth, the bubble flattens to form a "pancake" shape.[12] Typical images of spherical and pancake bubbles are shown in Fig. 1(a) and the pancake bubble shape is shown schematically in Fig. 2. When the pancake diameter exceeds the channel width, the bubble fills the cross-section and elongates to form a "slug" (Figs. 1(b) and 3).[15]

If the gas volume fraction increases for a fixed bubble size, then the arrangement of bubbles in the channel also depends on the microchannel geometry. Previous studies report five distinct types of monodisperse bubbly structures that can be formed in microfluidic devices: dripping (Fig. 1(a)), slugs (Fig. 1(b)), alternating foam (Fig. 1(c)), packed foam (Fig. 1(d)), and bamboo foam (Fig. 1(e)).[7,15] Dripping (Fig. 1(a)) is defined as a single row of bubbles equally spaced along the centerline of the channel and applies to both spherical and pancake bubbles.[7] Slugs (Fig. 1(b)) are essentially the same as dripping, but the bubble shape is that of a slug.[15] Alternating foam (Fig. 1(c)) occurs at higher gas volume fractions when the bubbles can no longer fit within a single row and must stagger to form multiple rows. If the volume fraction increases further, the bubbles will adopt a packed structure (Fig. 1(d)), where the bubble cross sections must deviate from circular to fit into the confined space.[14] Finally, the bubbles will pack together to form a ladder-like structure denoted "bamboo foam" for a single row of packed slug-shaped bubbles (Fig. 1(e)).[7]

When monodisperse bubbles are less confined, they arrange into well-ordered structures. At low gas volume fractions, the foam structure is similar to the packing of hard spheres in a small gap between two planar surfaces. The formation of two-dimensional "crystals" containing spherical microbeads has been studied by Kumacheva *et al.*, who characterized the packing structure as function of the ratio of microchannel width to bead size for a constant microchannel height.[16] In another example of the influence of the microchannel width, Yang *et al.*[17] characterized the dynamic structures of droplets after formation as a function of outlet geometry
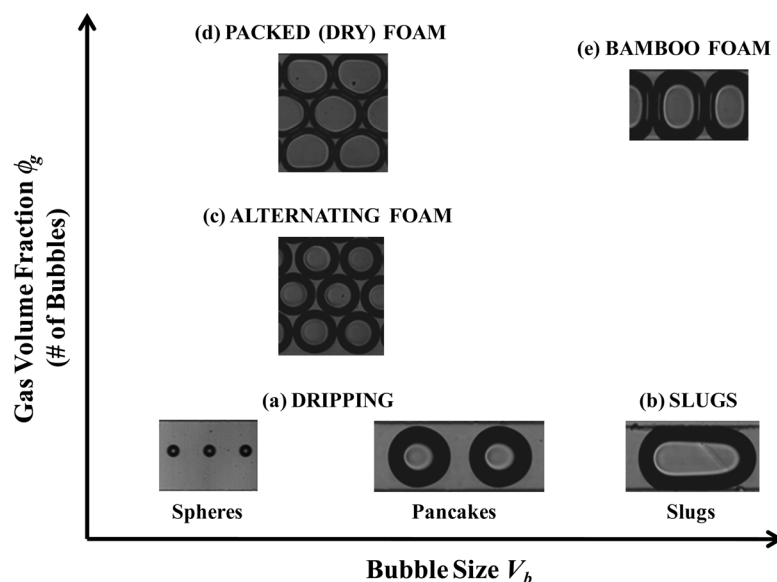

FIG. 1. Typical images of bubble shapes and structures, qualitatively organized in terms of gas volume fraction and bubble size.
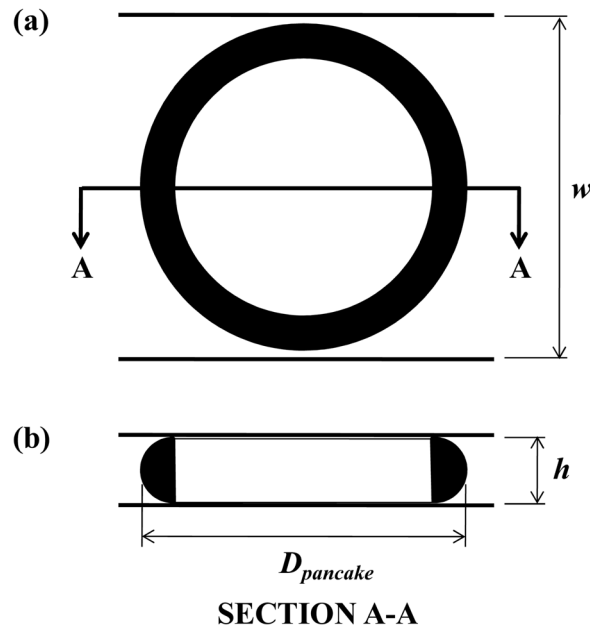
FIG. 2. Schematic diagrams of (a) top and (b) side views of a pancake bubble in a microchannel where $w > h$.

immediately after the nozzle. The authors found that different pancake-shaped droplet structures, corresponding to those that we denote dripping and alternating foam, formed depending on the shape of the expansion area between the nozzle and the final rectangular cross-section. The packing transition from two to three dimensions was observed by Pieranski et al. and characterized as a function of separation distance between the two confining surfaces.[18] A change in the total length of the channel will also induce a change in the structure, as described in compression studies performed by Fleury et al.[19] In three-dimensional space, Hatch et al.[3] examined the packing of approximately 50 μm spheres into multiple layers of droplets in a large microfluidic collection chamber. The generated droplets self-assembled into various packing configurations, including hexagonally close packed and cubic close packed. The authors considered microchannel dimensions much larger than the drop diameter and intermediate volume fractions ($\phi > 0.5$) in which the bubbles assembled but remained spherical. At higher gas volume fractions, the shape deformation from a sphere must be taken into account in the packing of bubbles. Two studies by Garstecki and Whitesides describe the possible periodic structures of dry foams that are comprised of individual bubbles whose shapes deform to minimize the local interfacial energy.[20,21] Foams formed at higher flow rates adopt higher energy structures. Hashimoto et al.[43] showed that the combination of multiple bubble and droplet generators gives rise to foams and emulsions consisting of inclusions of varying size and composition that will also adopt periodic structures.

In confined geometries, the conditions at which a foam transitions from one structure to another strongly depend upon the microchannel geometry, the volume of the bubbles V_b, and the gas fraction ϕ_g. In the present study, we will characterize the bubble shape and foam structure using these two parameters in rectangular microchannels with dimensions comparable to the bubble size. A geometric model will be developed to describe the expected bubble shapes and structures. In the discussion that follows, we will use the terms "bubble" and "droplet," and the terms "foam" and "emulsion" interchangeably. Although there are differences between the two, the geometric arguments that we present here apply equally well to both. The critical bubble volumes and volume fractions defining the transitions between structures will be determined and used to generate a regime map for a given channel aspect ratio. The predicted regime maps will be compared with experiments corresponding to several microchannel aspect ratios, various component fluids, and three different nozzle types. The experiments and model encompass
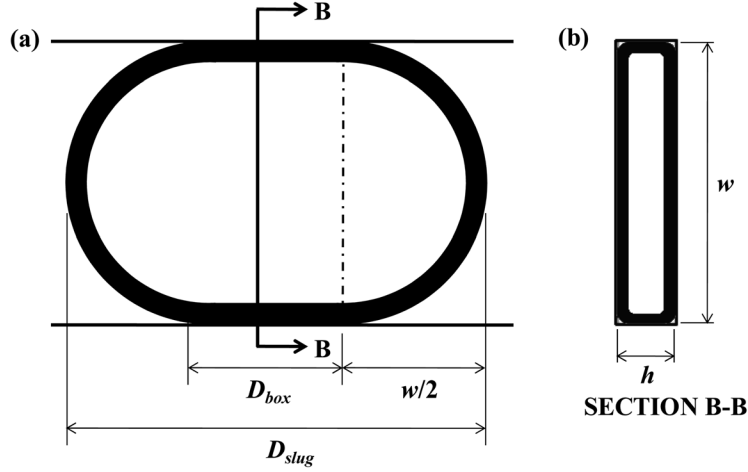
FIG. 3. Schematic diagrams of (a) top and (b) side views of a slug bubble in a microchannel where $w > h$.

bubble volumes from 10^{-2} to 10^2 nl and gas volume fractions from 0.01 to 1, covering the full spectrum of possible monodisperse foam structures.

II. GEOMETRIC MODEL FOR FOAM STRUCTURE

In this section, we develop a simplified model describing the structure of a foam containing a uniform bubble size that is confined within a rectangular microchannel. We outline the approach here along with the resulting expressions describing transitions between different bubble sizes and foam structures. Additional details are available in the supplementary material.[22] We assume that the channel depth h is less than or equal to the width w, and that the channel length L is significantly longer than either of these two dimensions ($h \leq w \ll L$). The underlying hypothesis is that the foam structure is independent of the manner in which it is produced. In other words, we consider static conditions and neglect the influence of nozzle type, flow conditions, fluid properties (e.g., viscosity and interfacial tension), and channel wall material. We therefore develop geometric arguments for the foam structure, first defining each bubble shape transition, followed by each bubble structure transition.

Assuming that a bubble will attain a spherical shape if unbounded, the bubbles will remain spherical until the diameter of the bubble D_{sphere} exceeds the depth of the channel

$$D_{sphere} \geq h. \tag{1}$$

Larger bubbles will be confined by the top and bottom walls of the microchannel and will adopt a pancake-like shape as shown schematically in Fig. 2. Expressing the diameter of the bubble in terms of its volume, the critical bubble volume $V_{b,sp}$ at which the sphere to pancake transition occurs is given by

$$V_{b,sp} = \frac{\pi}{6} h^3. \tag{2}$$

Approximating the shape of a pancake bubble as a cylinder surrounded by a semi-circular cap, as shown in Fig. 2(b), the volume is estimated by

$$V_{pancake} = \frac{\pi h^3}{6} + \frac{\pi h}{4} (D_{pancake} - h) \left(\frac{\pi h}{2} + D_{pancake} - h \right). \tag{3}$$

When the projected diameter of a pancake bubble obtained from Eq. (3) exceeds the width of the channel,

$$D_{pancake} \geq w, \tag{4}$$

the bubble becomes elongated into a slug-like shape. Substituting Eq. (3) into Eq. (4) reveals a critical volume $V_{b,ps}$ at which the pancake to slug transition occurs,

$$V_{b,ps} = \frac{\pi}{8} wh[(\pi - 4)h + 2w] + \frac{\pi}{24} h^3 (10 - 3\pi). \tag{5}$$

It should be noted that the critical volumes for both shape transitions (Eqs. (2) and (5)) depend only on the channel dimensions.

   Once the bubble volume has exceeded the critical value $V_{b,ps}$, the bubble is confined by all four walls of the channel, thereby adopting a cross-sectional shape that conforms to that of the channel (Fig. 3(b)). The slug will adopt a finite radius of curvature in the corners of the rectangular cross-section due to surface tension. We neglect the small volume in the corners in our estimates, but note that the corners will strongly influence the speed at which the bubbles flow along the channel.[23,24] The slug shape can be approximated as a box with two half-pancake endcaps, where the diameter $D_{pancake}$ is equal to the width of the channel w. The resulting estimated length of the slug bubble D_{slug} (Fig. 3(a)) along the axis of the microchannel in terms of channel dimensions and bubble volume V_b is given by

$$D_{slug} = w + \frac{1}{wh} \left\{ V_b - \left[\frac{\pi h^3}{6} + \frac{\pi h}{4} (w - h) \left(\frac{\pi h}{2} + w - h \right) \right] \right\}. \tag{6}$$

   In addition to bubble shape transitions, there are also bubble structure transitions that are functions of gas volume fraction, ϕ_g. The bubble structure is determined by the spatial arrangement of the bubbles in the available channel volume. The number of bubbles n_b that corresponds to a specified gas volume fraction can be estimated as

$$n_b = \frac{\phi_g whL}{V_b}. \tag{7}$$

For a fixed bubble size, the bubbles rearrange to fit within the channel as the gas fraction increases. At low gas fractions, bubbles form a single, uniformly spaced row of bubbles. This is the structure that we term "dripping."[7] The center-to-center distance or spacing s between bubbles is given by

$$s = \frac{V_b}{\phi_g wh}. \tag{8}$$

As the volume fraction increases, the spacing decreases.

   When the spacing given by Eq. (8) is less than the projected diameter of the spherical or pancake bubble,

$$s \leq D_{projected}, \tag{9}$$

the bubbles can no longer form a single row, and they begin to stagger to occupy additional rows, forming the structure that we call "alternating foam."[7] The critical volume fraction at which the structure transitions from dripping to alternating foam is given by

$$\phi_{g,da} = \left(\frac{\pi}{6} \frac{V_b^2}{w^3 h^3} \right)^{1/3}, \tag{10a}$$

for spherical bubbles and

$$\phi_{g,da} = \frac{V_b}{wh^2 \left[\left(\frac{4}{\pi} \frac{V_b}{h^3} + \frac{\pi^2}{16} - \frac{2}{3} \right)^{1/2} - \frac{\pi}{4} + 1 \right]}, \tag{10b}$$

for pancake bubbles.

Alternating foam occurs when the number of rows of bubbles is greater than one. The number of rows n is determined by taking the ceiling of the number of channel lengths L required to fit all the bubbles into one row with the spacing equal to the projected bubble diameter

$$n = ceiling\left(\frac{n_b D_{projected}}{L}\right). \tag{11}$$

Equation (11) indicates that any fraction of a row will form an additional row. The larger the decimal in the argument of n, the smaller the center-to-center distance between bubbles in a given row. The spacing s can be calculated by combining Eqs. (7) and (8) and accounting for multiple rows

$$s = \frac{nL}{n_b}. \tag{12}$$

As the volume fraction increases, the bubbles will fill up one row and form additional rows as necessary to maintain their circular shape. This will occur whether the bubbles have increased in size or in number. The maximum packing configuration that allows the projected shape of the bubbles to remain circular is a 2D hexagonal close packed structure, illustrated schematically in Fig. 4. In this densely packed structure, the center-to-center spacing s in any one row of bubbles is given by

$$s = D_{projected}, \tag{13}$$

and the center-to-center distance between bubbles in adjacent rows is $(\sqrt{3}/2)D_{projected}$. For a given number of rows, there is a maximum bubble size that can be achieved before the bubble shape must deform to fit within the confines of the channel. The transition between alternating to packed foam occurs when the total width of all bubble rows exceeds the width of the microchannel w, leading to a critical bubble volume given by

$$V_n = \frac{\pi}{6}\left[\frac{2}{\sqrt{3}(n-1)+2}\right]^3 w^3, \tag{14a}$$

for spherical bubbles and

$$V_n = \pi \frac{h^3\alpha(10-3\pi) + 2wh^2\{\sqrt{3}(n-1)[2wh^2(10-3\pi)+3(\pi-4)]+6(\pi-4)\}+24}{24[\alpha+4\sqrt{3}(n-1)]}, \tag{14b}$$

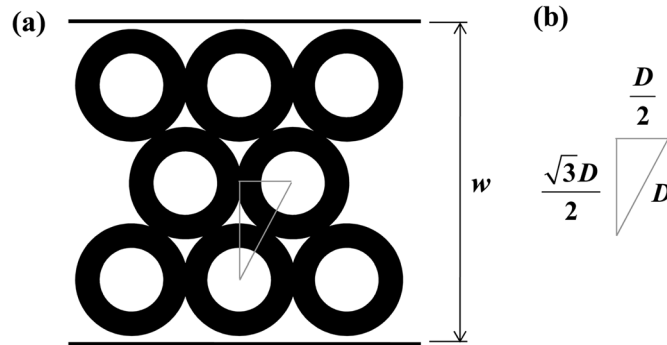for pancake bubbles, where $\alpha = 3n(n-2)+7$.

FIG. 4. Schematic diagram depicting the arrangement of bubbles occupying multiple rows in a two-dimensional hexagonal close packed pattern in a microchannel of width w.

Note that for a given number of rows, the critical volume at which a foam transitions from alternating to packed is independent of volume fraction. However, there is an additional consideration needed to fully describe this transition. The transition is also defined by the maximum number of rows that can physically fit within the width of the microchannel, yielding a critical volume fraction at which the bubble structure transitions from alternating to packed foam given by

$$\phi_{g,ap} = n_{\max} \left(\frac{\pi}{6} \frac{V_b^2}{w^3 h^3} \right)^{1/3}, \tag{15a}$$

for spherical bubbles and

$$\phi_{g,ap} = n_{\max} \frac{V_b}{wh^2 \left[\left(\frac{4}{\pi} \frac{V_b}{h^3} + \frac{\pi^2}{16} - \frac{2}{3} \right)^{1/2} - \frac{\pi}{4} + 1 \right]}, \tag{15b}$$

for pancake bubbles, where $n_{\max} = 2(w - D_{projected})/\sqrt{3} D_{projected} + 1$ is the maximum number of rows of bubbles that can fit within a microchannel. Note that Eqs. (15a) and (15b) account for multiple rows of bubbles and are the more general forms of Eqs. (10a) and (10b).

These transitions also exist for slug bubbles, where the number of rows $n = 1$. The slug regime is analogous to the dripping regime, and slugs will transition directly to a single row of packed foam, denoted "bamboo foam." The transition between slugs and a single row of packed foam occurs when the center-to-center spacing s is shorter than the projected length of the slug bubble D_{slug}

$$s \geq D_{slug}. \tag{16}$$

The resulting critical gas volume fraction at which slugs will transition to bamboo foam is

$$\phi_{g,sb} = \frac{V_b}{V_b + \left(1 - \frac{\pi}{4} \right) \left(w^2 h + \frac{\pi}{2} wh^2 \right) + \frac{\pi}{2} \left(\frac{\pi}{4} - \frac{5}{6} \right) h^3}. \tag{17}$$

Note that this definition of bamboo foam is slightly different from what is qualitatively observed and named bamboo foam by Raven et al.[7] By our definition, a single row of packed foam is distinguished from bamboo foam. In a single row of packed foam, the projected circular diameter of the bubble can be smaller than the width of the microchannel, while in bamboo foam, this projected diameter must always be larger than the width of the microchannel. These two scenarios are equivalently termed bamboo foam in the literature.[7] Our definition of bamboo foam typically occurs at larger bubble volumes than what has been previously described qualitatively.

The shape and structural transitions given by Eqs. (2), (5), (10), (14), (15), and (17) can be written in dimensionless form, defining a dimensionless bubble volume by $V^* \equiv V_b/w^2 h$ and the channel aspect ratio $\Lambda \equiv h/w$. The resulting expression for the critical volume at which the spherical to pancake shape transition occurs is given by

$$V_{sp}^* = \frac{\pi}{6} \Lambda^2, \tag{18}$$

while the critical volume for the pancake to slug shape transition is described by

$$V_{pb}^* = \frac{\pi}{4} \left(\frac{10 - 3\pi}{6} \Lambda^2 + \frac{\pi - 4}{2} \Lambda + 1 \right). \tag{19}$$

The critical volume fraction at which the bubble structure transitions from dripping to alternating foam to packed foam is given by

$$\phi_{g,dap} = n_{\max} \left(\frac{\pi}{6} \frac{V^{*2}}{\Lambda} \right)^{1/3}, \tag{20a}$$

for spherical bubbles and

$$\phi_{g,dap} = n_{\max} \frac{V^*}{\Lambda \left[\left(\frac{4}{\pi} \frac{V^*}{\Lambda^2} + \frac{\pi^2}{16} - \frac{2}{3} \right)^{1/2} - \frac{\pi}{4} + 1 \right]}, \tag{20b}$$

for pancake bubbles. The corresponding volume-fraction-independent transitions are defined by

$$V_n^* = \frac{\pi}{6} \left[\frac{2}{\sqrt{3}(n_{\max} - 1) + 2} \right]^3 \frac{1}{\Lambda}, \tag{21a}$$

for spherical bubbles and

$$V_n^* = \pi \frac{\alpha(10 - 3\pi)\Lambda^2 + 2\{\sqrt{3}(n_{\max} - 1)[2\Lambda(10 - 3\pi) + 3(\pi - 4)] + 6(\pi - 4)\}\Lambda + 24}{24[\alpha + 4\sqrt{3}(n_{\max} - 1)]}, \tag{21b}$$

for pancake bubbles. Finally, the critical volume fraction at the transition from slug to bamboo foam can be described by

$$\phi_{g,sb} = \frac{V^*}{V^* + 1 - \frac{\pi}{6}\Lambda^2 + \frac{\pi}{4}\left[\left(\frac{\pi}{2} - 1 \right)\Lambda^2 + \left(2 - \frac{\pi}{2} \right)\Lambda - 1 \right]}. \tag{22}$$

III. MATERIALS AND METHODS

To validate the geometric arguments outlined in Sec. II, we conduct experiments using microfluidic geometries to generate monodisperse bubbles and drops with various volumes and dispersed phase volume fractions. Three microfluidic geometries are used to form bubbles and droplets, (a) flow-focusing, (b) co-flow, and (c) T-junction devices. Each of these nozzle geometries have been described and characterized extensively.[6] In the flow-focusing and co-flow geometries, the dimensions used are $w_{in} = L_{in} = 200 \, \mu m$, $L_{out} = 10 \, mm$, and $w_{out} = \{100, 200, 400, 500, \text{ and } 1000\} \, \mu m$. The width of the orifice in the flow-focusing device is $w_{or} = 50 \, \mu m$. The dimensions of the T-junctions are such that both arms are approximately the same width and $w = \{100, 500, \text{ and } 1000\} \, \mu m$. The depth $h = \{80, 100, \text{ and } 200\} \, \mu m$ for all three geometries. The depth and width of each outlet channel are selected to correspond to one of the three aspect ratios considered: $\Lambda = 1$, 0.2, and 0.1.

All microfluidic devices are fabricated in poly(dimethylsiloxane) (PDMS) (Dow Sylgard 184) using standard soft lithography fabrication techniques.[4] The channels are sealed against a thin slab of PDMS to ensure that all four walls exhibit the same wetting characteristics. The dimensions listed above are the design dimensions. Fabricated in-plane dimensions were measured optically and found to be within $10 \, \mu m$ of the target dimensions. Channel depths were measured using a contact profilometer (Veeco Dektak) and found to be within $5 \, \mu m$ of the target depth. Swelling due to permeation of oil into the PDMS can also change these dimensions slightly and is assumed to change the dimensions by the same multiplicative factor in all directions. As a result, the aspect ratio is assumed to remain constant.

In the case of bubble formation, nitrogen gas is used as the dispersed phase fluid. The continuous phase liquid is de-ionized water containing 1%, 5%, or 10% w/w Triton X-100 (Sigma Aldrich T8532—for electrophoresis, used as received), which is a water soluble non-ionic surfactant with a critical micelle concentration (CMC) of 0.22 to 0.24 mM (manufacturer

specifications, Sigma-Aldrich). The presence of dissolved surfactant at such high concentrations is required for stable bubble formation. In the case of droplet formation, the dispersed phase is either pure de-ionized water or a 50/50 glycerol-water mixture. The continuous phase is either light mineral oil (Fisher Scientific) with a viscosity of $\mu = 40$ cP or silicone oil (Fluka) with a viscosity of $\mu = 6$ cP. Oil-soluble surfactant, Span 80 (Sigma Aldrich S6760, used as received), is dissolved in the oil phase at a concentration of either 0.67% or 10% w/w. Because monodisperse bubble and droplet formation is the goal of all the experiments, the exact fluid properties are not of particular interest and the fluids and surfactant concentrations are chosen to yield consistent, stable, monodisperse bubbles and droplets based on previous experience. Data from previously published work are also compared with the geometric arguments; the details are described elsewhere.[25]

The two parameters of interest are the droplet or bubble volume and the overall dispersed phase volume fraction. In practice, the fluid flow rates control both of these parameters and V_d and ϕ_d are measured using image analysis of high speed videos. For foams, a two-stage pressure regulator followed by a second electronic pressure regulator (ControlAir, Inc. T550X Miniature EIA) is used to control the nitrogen gas pressure, which varies between 15 and 35 kPa at the exit of the second regulator. Note that the input mass flow rate of gas is not controlled or measured in this experimental setup. Rather, the bubble volume and corresponding volume fraction are measured visually at a given location in the microchannel, as described below. The mass fraction will vary with bubble size since the Laplace pressure within a bubble increases with decreasing bubble size. For emulsions, the volumetric flow rates of the water and oil phases are controlled by separate syringe pumps (Harvard Apparatus PHD2000) and vary between 0.05 and 300 μl min^{-1}. All experiments are allowed to achieve steady state flow conditions for at least 15 min before images are recorded.

Bubble and droplet formation is visualized using an inverted microscope (Nikon TE2000U or Ti-U) with an attached high-speed camera (IDT XS5, Redlake or Phantom v9.1, Adept Turnkey Pty, Ltd.). Videos of the droplet or bubble formation process in addition to the downstream structure are captured digitally and individual images are analyzed using IMAGEJ (NIH 1.43 u). If the shape is approximately circular, the measured diameter is compared with the known channel depth. If the diameter exceeds the channel depth, the volume is determined assuming the shape is a pancake (Eq. (6)). If not, the volume is determined assuming the shape is a sphere. The measured volume fraction is obtained by taking the ratio of the total bubble volume and the total channel volume of interest. The total bubble volume is determined by multiplying the volume of one bubble or droplet by the number of droplets observed in a section of the microchannel. The total channel section volume is obtained by measuring the length of that section of the channel and multiplying it by the measured width and depth of the channel. Swelling effects are taken into account in the calculated total channel section volume. The foam or emulsion structure for a given experiment is determined by counting the number of rows, measuring the droplet or bubble spacing, and observing whether the shape is distorted by proximity to neighboring objects (i.e., another bubble or droplet or the channel walls). To determine the difference between alternating and packed foam, the ellipticity of the interface is estimated using image analysis. An ellipticity value ε close to 1.0 ($\varepsilon > 0.8$) is considered circular and values below $\varepsilon \leq 0.8$ are considered sufficient deviation from circular to denote the structure as packed.

IV. RESULTS

The dimensionless Eqs. (18)–(22) can be used to generate a regime map categorizing the bubble shapes and structures expected as a function of dimensionless bubble volume V_b^* and gas fraction ϕ_g for a fixed channel aspect ratio Λ. The geometric arguments outlined here result in transitions that depend only on bubble size, gas volume fraction, and channel geometry. Therefore, the criteria should apply to any dispersed phase fluid, including liquid droplets dispersed in an immiscible liquid. To generalize Eqs. (18)–(22), the bubble volume V_b^* is replaced with the dispersed phase volume V^* and the gas volume fraction ϕ_g is replaced with the

dispersed phase volume fraction ϕ_d. Similarly, the predicted transitions are independent of the nozzle shape or method of formation of the drops or bubbles prior to entering the channel. A typical regime map corresponding to an aspect ratio of $\Lambda = 0.2$ using these renamed variables is shown in Fig. (5). The figure is plotted on a log-log scale where the horizontal axis is the dimensionless bubble or droplet volume V^*, and the vertical axis is the dispersed phase volume fraction ϕ_d. Both axes span several orders of magnitude but have a physical lower limit of zero, which corresponds to a pure medium. The bubble or droplet volume has no numerical upper limit, as the bubble volume can be much larger than the unit volume $w^2 h$ of channel. However, the upper limit of the volume fraction ϕ_d is unity because the dispersed phase volume cannot be greater than the total volume.

In Fig. (5), the lines represent the critical conditions for each transition given by Eqs. (18)–(22). Each region of operating space is labeled with the corresponding shape and structure. The critical dimensionless bubble volumes are the solid vertical lines that divide the regime map into three bubble shape regions corresponding to spheres, pancakes, and slugs in order of increasing volume. For this aspect ratio, the critical dimensionless bubble volume defining the expected transition from spherical to pancake bubbles is $V_{sp}^* = 0.02$, which is indicated by the left most vertical line on the figure. Similarly, $V_{ps}^* = 0.72$ is the critical volume defining the expected transition from pancake to slug bubbles. The critical bubble volume fractions that divide each shape region into smaller regions defining the structure are functions of the dimensionless bubble volume and the channel dimensions. The transitions pertaining to spheres are shown as dotted lines, those corresponding to the pancakes are shown as solid lines, and the single structure transition for the slug bubbles is shown as a dashed line. In order of increasing volume fraction, the regions correspond to dripping, alternating, and packed foam for sphere and pancake shapes, and slugs and bamboo foam for slug shapes. Furthermore, the alternating to packed foam transition appears as a sawtooth line for each integer jump in the maximum number of rows. The sawtooth pattern reflects the two components of the transition; one that
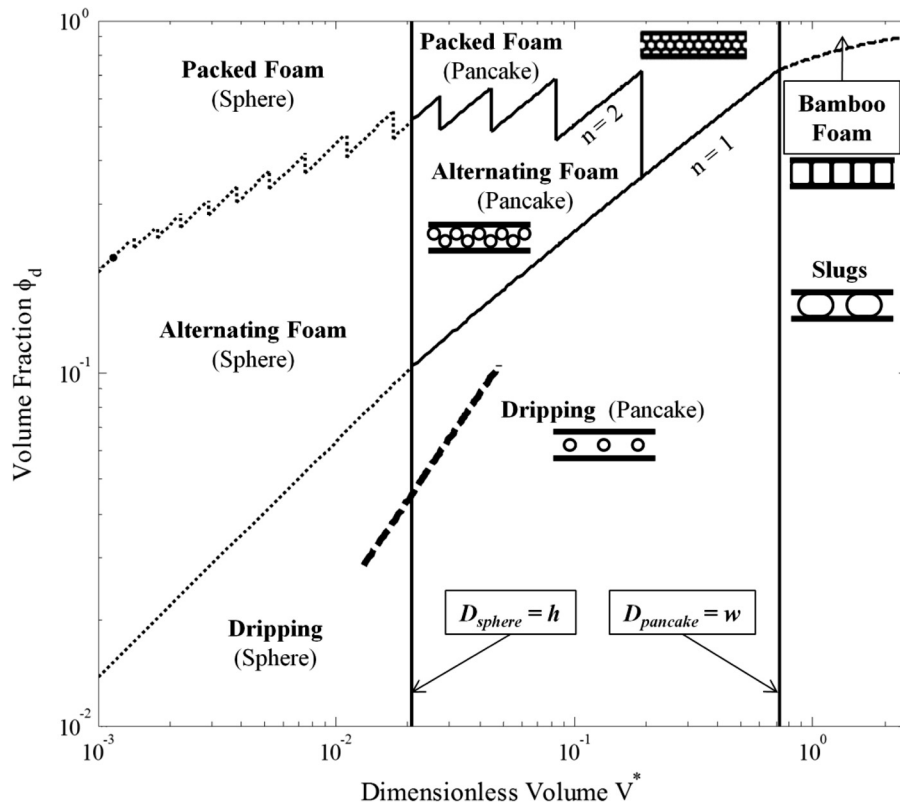

FIG. 5. Predicted regime map of bubble shapes and structures in a rectangular microchannel with $\Lambda = 0.2$.

depends only on the bubble volume (vertical lines), and one that depends on both bubble volume and volume fraction (slanted lines).

The operating space described here depends purely on the local bubble volume and volume fraction at a given position along the length of a microchannel. However, in a pressure-driven microchannel flow, there is a linear pressure decrease along the length of the channel. This implies that the volume of a bubble containing compressible gas will increase along the length of the channel, which will in turn change both the volume fraction and the resulting foam structure. Since the pressure drop along a microchannel depends on flow rate and flow resistance of the foam within a channel, the volume-volume fraction trajectory followed by a given bubble depends on the flow rate and the foam structure, which can significantly influence the flow resistance. To illustrate the concept, we consider small, spherical bubbles in which the bubbles themselves do not contribute significantly to the flow resistance in the channel. Assuming that the bubbles contain an ideal gas and that the flow resistance arises from a Hagen-Poiseuille-like relationship for a Newtonian fluid in a rectangular channel, the changes in bubble volume and gas volume fraction along the channel can be estimated. The dashed line shown in Fig. 5 shows an example of a volume-volume fraction trajectory for a spherical bubbly structure that starts in the dripping mode and travels along a 1 m length of microchannel. Note that the length over which this trajectory is estimated is longer than the typical length of a microchannel and that the bubble volume changes by less than 3% over a typical microchannel length (10 mm). However, once the bubble volume and volume fraction are large enough to contribute to the flow resistance, the calculation of the changes in volume and volume fraction along the channel becomes more complicated.[26,27] Droplets are generally considered incompressible and, therefore, would not exhibit a volume change arising from the pressure drop in the channel.

Equations (18)–(22) are applicable to any pair of immiscible fluids and any nozzle type, which is reflected in the chosen experimental systems. To compare with the geometric transitions predicted in Fig. 5, we determine the volumes and volume fractions for a wide range of emulsions and foams generated using flow-focusing and co-flow microfluidic devices with downstream aspect ratios equal to $\Lambda = 0.2$. Nitrogen bubbles in water containing dissolved Triton X-100 comprise the foams that are studied. The emulsions consist of deionized water drops in a continuous phase of mineral oil containing dissolved Span 80. The bubbles and droplets generated are monodisperse and stable during the time the bubbles or droplets travel the length of the channel (1–10 s). For each bubble volume and volume fraction achieved in experiments, the bubble shape and structure is determined using the image analysis protocols outlined in Sec. III. The results are shown in Fig. 6 along with the same predicted transitions shown in Fig. 5. The three data points lying between $10^{-3} < V^* < 10^{-2}$ at the dripping to alternating foam transition line are included from case B of Ref. 25, which corresponds to drops of water with dissolved octaethylene glycol monododecyl ether ($C_{12}E_8$) surfactant in light mineral oil, as described in Sec. III.[25]

In Fig. 6, there are two symbol fills to represent the two nozzle types used to generate the foams and emulsions for this aspect ratio: filled symbols represent flow-focusing data and x-filled symbols represent co-flow data. The regimes that are represented experimentally include dripping ($\Diamond$) for both spheres and pancakes, slugs ($\Box$), alternating foam ($\bigcirc$) for both spheres and pancakes, packed foam (Δ) for pancakes, and bamboo foam (∇). The same symbols are used to represent the structures for spheres and pancakes because we could not experimentally observe this shape transition in the top-down view of the microscope. We assume that the bubbles are pancake-shaped if the diameter is greater than the channel depth. The only regime not represented experimentally for the aspect ratio $\Lambda = 0.2$ is the packed foam structure consisting of spherical bubbles. Attempts to reach this region of the regime map experimentally result in either no bubble or droplet break-up or larger bubbles and droplets.

Fig. 6 indicates that for most experimental conditions, the bubble shape and foam structure observed for a given bubble volume and volume fraction are the same as that predicted by the geometric arguments of Eqs. (18)–(22) for an aspect ratio $\Lambda = 0.2$. Again, the sphere to pancake transition was not experimentally observable, so we have not verified this shape transition. The pancake to slug shape transition, however, is easily visualized with our experimental setup.
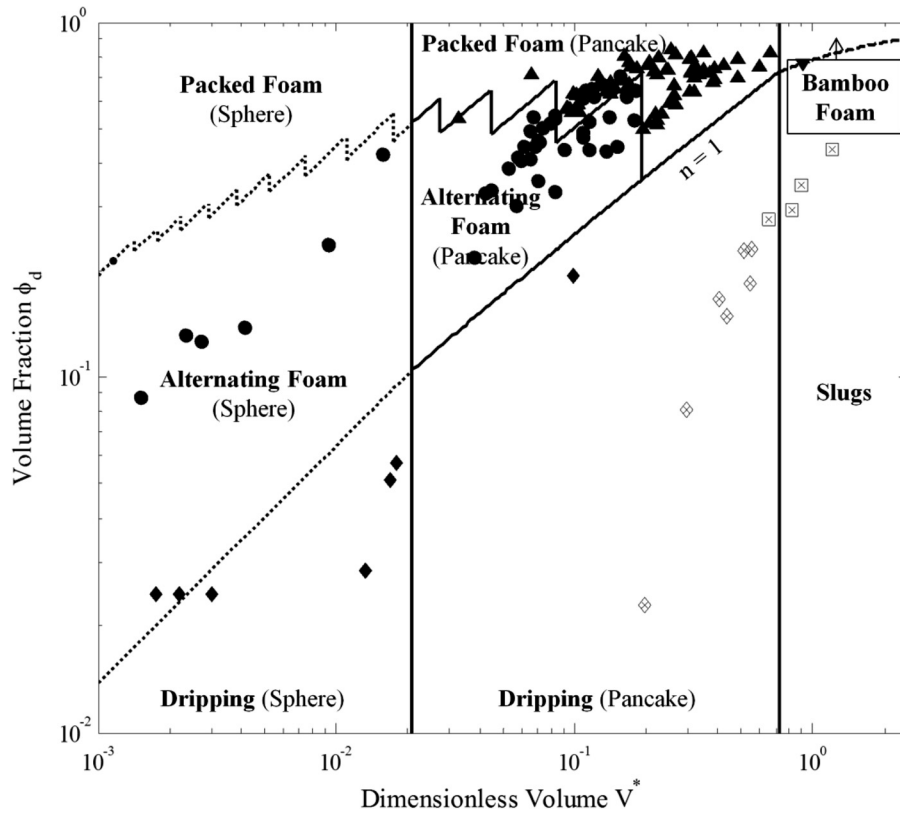
FIG. 6. Regime map of observed and predicted dispersed phase shapes and structures in a rectangular microchannel ($\Lambda = 0.2$). Symbol fill indicates the nozzle type: filled symbols—flow-focusing, open symbols—T-junction, and x-filled symbols—co-flow. Symbol shapes indicate structure: ($\Diamond$) dripping, ($\Box$) slugs, ($\bigcirc$) alternating foam, ($\triangle$) packed foam, and (∇) bamboo foam.

There is good agreement with the model in cases where the bubble volumes are not near the critical volume for a shape transition, as seen by experimental data symbols lying within the corresponding shape region of the regime map. Near the critical bubble volume, $V_{ps}{}^* = 0.72$, there is one inconsistent data point, where the shape is predicted to be a pancake bubble, but is categorized as a slug bubble ($\Box$).

The structure transitions are similarly easy to visualize as they occur. Away from the transition lines, there is again good agreement between the predicted and observed foam structures. There are a few discrepancies near the predicted transitions. At the dripping to alternating transition for spheres, there are two data points that exhibit a dripping structure ($\Diamond$) but are expected to form an alternating foam. At the alternating to packed foam transition at $n = 2$ rows for pancakes, there are several data points that are observed to exhibit an alternating foam structure ($\bigcirc$) but are expected to form a packed foam instead.

The geometric arguments suggest that the bubble shape and foam structure regimes depend on channel aspect ratio. For example, the critical dimensionless bubble volume for the transition from spherical to pancake bubbles occurs at $V_{sp}{}^* = 0.005$ for an aspect ratio $\Lambda = 0.1$, which is significantly smaller than the same transition for the aspect ratio $\Lambda = 0.2$. The pancake to slug transition occurs at $V_{ps}{}^* = 0.75$ for $\Lambda = 0.1$, which is slightly larger than the same transition for $\Lambda = 0.2$. Thus, the region of parameter space in which we expect to observe pancake-shaped bubbles grows wider as the aspect ratio decreases. All expected structure transitions are still present in the reduced aspect ratio case but have shifted from those presented in Figs. 5 and 6 for $\Lambda = 0.2$. The transitions from dripping to alternating foam, alternating to packed foam, and slug to bamboo foam occur at increasing volume fractions for a fixed volume as the aspect ratio decreases. A distinct difference between the aspect ratios $\Lambda = 0.2$ and $\Lambda = 0.1$ is the increase in
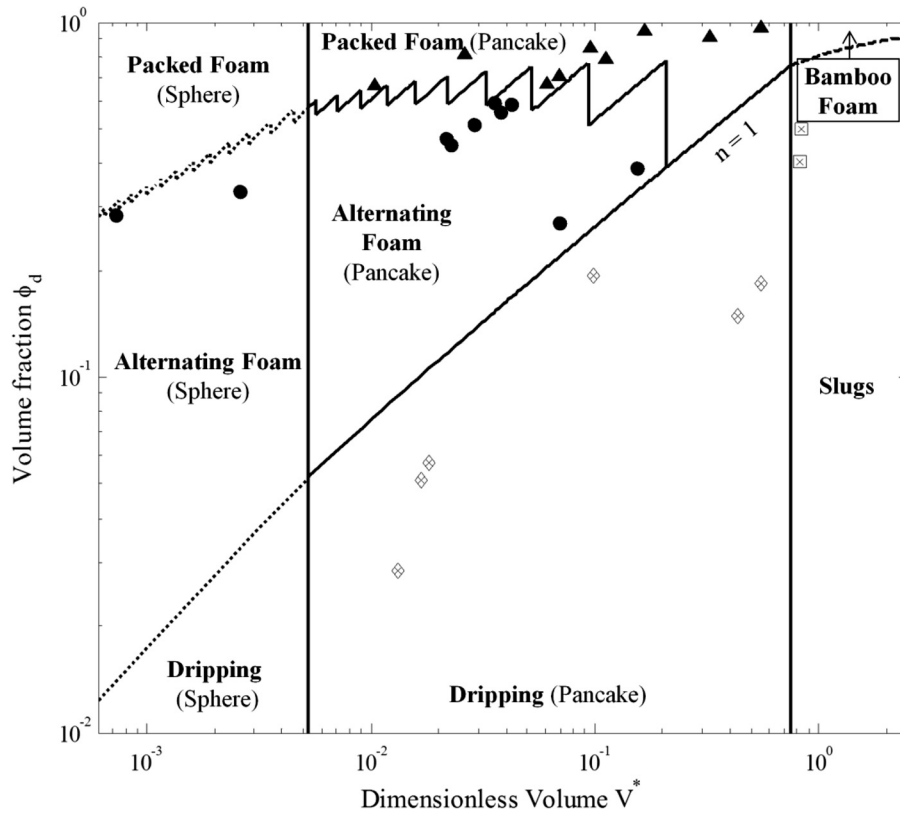
FIG. 7. Regime map of observed and predicted dispersed phase shapes and structures in a rectangular microchannel ($\Lambda = 0.1$). Symbol fill indicates the nozzle type: filled symbols—flow-focusing, open symbols—T-junction, and x-filled symbols—co-flow. Symbol shapes indicate structure: ($\Diamond$) dripping, ($\Box$) slugs, ($\bigcirc$) alternating foam, (Δ) packed foam, and (∇) bamboo foam.

the number of rows of pancake bubbles that can be accommodated across the microchannel before they become distorted. The limits on the axes of the phase diagram remain the same as before. The predicted shape and structure transitions are shown for $\Lambda = 0.1$ in Fig. 7.

We conducted experiments using flow-focusing and co-flow nozzles to generate emulsion drops in channels with aspect ratio $\Lambda = 0.1$. The emulsions consisted of deionized water droplets in mineral oil containing 10% w/w Span 80. Using the same symbols shown in Fig. 6, the bubble and droplet shapes that are represented experimentally include all three shapes, while the structure regimes represented include pancake dripping ($\Diamond$), slugs ($\Box$), alternating foam ($\bigcirc$) for both spheres and pancakes, and pancake packed foam (Δ). The regions that are not experimentally observed are dripping and packed foams of spheres and bamboo foam. Bubble and droplet formation is experimentally unstable in these regions and did not generate stable monodisperse bubbles or droplets. For the shape and structure regions that are experimentally represented, the data show good agreement with predicted regimes. The observed emulsion and foam structures match the expected shapes and structures for the corresponding volume and volume fraction, even near the critical dimensionless bubble volumes and volume fractions.

For an aspect ratio of $\Lambda = 1$, the channel cross-section is square, implying that the droplet or bubble shape will transition directly from spheres to slugs, which is reflected in the collapse of the pancake region observed in Fig. 8. As such, the one vertical line in this figure at a dimensionless bubble volume $V_{sp}^* = V_{ps}^* = 0.52$ represents the predicted critical volume where the sphere to slug shape transition will occur. All of the bubble structures are still present in the predicted regime map, with the exception of those associated with the pancake region. Another distinct difference between the previous two regime maps ($\Lambda = 0.2$ and 0.1) and this one ($\Lambda = 1$) is the presence of a single row packed foam regime at smaller spherical bubble volumes to the left of the transition to bamboo foam at larger bubble volumes, which is present
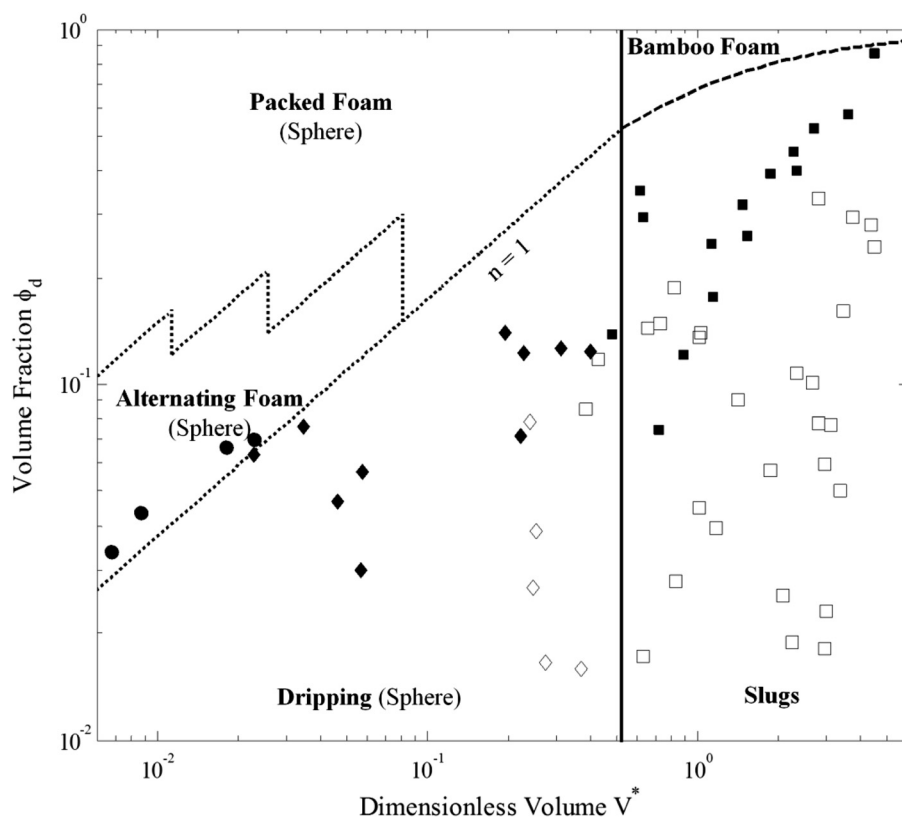
FIG. 8. Regime map of observed and predicted dispersed phase shapes and structures in a rectangular microchannel ($\Lambda = 1$). Symbol fill indicates the nozzle type: filled symbols—flow-focusing, open symbols—T-junction, and x-filled symbols—co-flow. Symbol shapes indicate structure: ($\diamond$) dripping, ($\square$) slugs, ($\bigcirc$) alternating foam, ($\triangle$) packed foam, and (∇) bamboo foam.

only in the pancake-shaped packed foam regime at lower aspect ratios. The limits of the axes otherwise remain the same. The square cross-section is an important physical limit of the microchannel geometry. The depth of the channel can exceed the width, but the two parameters could then be interchanged and the same transitions would still apply. The square microchannel ($\Lambda = 1$) is, therefore, the upper limit of the aspect ratio on the geometric model and yields a distinctly different phase diagram compared with aspect ratios less than unity.

The shape and structure transitions plotted in Fig. 8 are experimentally verified using flow-focusing and T-junction nozzles to generate water-in-oil emulsions. Here, flow-focusing data continue to be represented by filled symbols, and the T-junction data are represented by open symbols. For the flow-focusing experiments, the emulsions are comprised of deionized water in mineral oil containing 10% w/w Span 80. The droplets generated in T-junctions contain either deionized water or glycerol-water (50/50) solutions in a continuous phase of mineral oil or silicone oil. Experiments with and without 0.67% Span 80 in the oil phase are also carried out in the latter nozzle design. Using these experimental conditions, data are obtained in the dripping ($\diamond$), slugs ($\square$), and alternating foam ($\bigcirc$) regimes for the aspect ratio $\Lambda = 1$. Data could not be obtained for packed foams with spherical inclusions or for bamboo foam due to either unstable bubble or droplet break-up or none at all.

Comparison of the geometric model and the experimental data for an aspect ratio of $\Lambda = 1$ (Fig. 8) shows that the observed shapes and structures that reside away from the transition lines match the predictions for the corresponding volumes and volume fractions. At the sphere to slug transition, there are three data points (one from a flow-focusing nozzle and two from a T-junction nozzle) that have been characterized as slugs but lie in the sphere region. The available data for dripping and alternating foams correspond well to the expected structures.

V. DISCUSSION

The geometric model described in Sec. III predicts that the bubble shape and structure of a foam confined within a rectangular microchannel will vary with the microchannel aspect ratio. This dependence is confirmed in Figs. 6–8. As the aspect ratio increases up to unity, the region containing pancake-shaped bubbles decreases in breadth until it completely disappears for a square microchannel. The critical volume fractions defining the structure transitions decrease for a given bubble volume as the aspect ratio increases, but all structures are observed for each aspect ratio. The experimental data and predicted regime maps presented in Figs. 6–8 agree relatively well for both bubbles and droplets generated using three nozzle types for the microchannel aspect ratios ($\Lambda = 0.1$, 0.2, and 1) studied here. More specifically, the geometric model predicts the shape and structure of the bubbles and droplets reasonably well for observed bubble volumes and volume fractions away from the critical values that indicate a transition between shapes or structures for all three aspect ratios discussed here. We observed a few discrepancies between the model and experiments in two of the aspect ratios ($\Lambda = 0.2$ and 1) near the pancake-to-slug (sphere-to-slug for $\Lambda = 1$) shape transition and at both the dripping to alternating foam and the alternating to packed foam structure transitions. The discrepancies between the model and the experimental data for these aspect ratios (Figs. 6 and 8) indicate that there are additional aspects of the physical systems that have not been taken into account.

The experimental procedure used to make comparisons with the geometric model has several limitations. For example, a cross-sectional view of the microchannel is not imaged, so the actual depth of the microchannel is unknown and the experimental critical volume at which a bubble or droplet deforms from a sphere to a pancake shape cannot be detected. This also affects the reported value of the dimensionless bubble volume, which requires knowledge of the actual microchannel dimensions. Since we do not know the local channel depth, we assume that the contact profilometer measurement provides an accurate average depth value for the microchannel. In addition, the model of the pancake shape, which currently assumes that the shape is a cylinder with a semi-circular endcap, is approximate and cannot be verified without a cross-sectional view of the channel. In general, error in the assumed shape contributes to the error in the reported bubble volume.

Another potential source of error arises from low image quality when capturing the bubble or droplet formation. Insufficient frame rates and low image contrast can cause difficulty with subsequent image analysis. For example, frame rates that are too slow to resolve the motion of the bubble or droplet along the channel produce blurry images, while insufficient image contrast leads to poor threshold limits for conducting edge detection analysis. Both of these issues affect the accuracy of bubble volume and ellipticity calculations. In the experiments corresponding to the alternating to packed foam structure transition in the pancake region for the aspect ratio $\Lambda = 0.2$ (Fig. 6), low image quality made it difficult to determine the ellipticity of the bubbles using digital image analysis. Instead, we visually estimate when deformation of the bubble interface was significant enough between alternating and packed foam for the bubble structure. Low image quality is likely the primary reason for blurring of the boundary between these two regions for experiments at $\Lambda = 0.2$.

Overall, the accuracy of the geometric model is surprisingly good given its simplicity. However, it does not describe all experimental conditions. For example, we assume that the foam is static even though flow is used to generate the bubbles and droplets, and the structures are typically still moving when imaged. In reality, the short length of channel (10 mm) coupled with the rapid formation and flow of the surfactant-stabilized structure along the length of the microchannel (residence times ≈ 1 s) does not allow for significant volume or structure change in the imaging time. We assume the observed structures are equivalent to the static counterpart for the same bubble volume and volume fraction. For emulsions, the input volumetric flow rates and the image analysis provide independent measures of the volume fraction. For foams, the volume fraction is obtained solely from image analysis since gas is input through a constant pressure source and the input mass flow rate is not controlled or measured. In both cases, we use the visually measured volume fraction rather than the input volumetric flow rate fraction

since the two are not necessarily equal during flow, even in the case of (incompressible) emulsions. This assumption works well for cases that are not too close to transitions. However, the flow can distort the shape away from the circular shape that we assume. Flow-induced distortion is particularly evident in experiments observed near the pancake to slug shape transition. Pancake-shaped bubbles will adopt a distorted shape even before the volume is large enough to be deformed by the channel walls. A variety of possible bubble and drop shapes induced by pressure driven flow in capillaries have been reviewed by Olbricht and calculated asymptotically by Nadim and Stone.[15,28] Garstecki and Whitesides have also commented on the effect of flow on the shape and structure that a foam will subsequently adopt.[20,21] The deformation of the bubble or droplet shape can also change as the foam or emulsion flows down the channel, which allows time for the inclusions to rearrange and find a lower energy state. Additional information on the specific shapes of the bubbles that comprise a dry foam can be found elsewhere.[29] Shape distortion by flow can induce error in the measured bubble volume and volume fraction as well as in the classification of the structure.

We assume that the fluid properties do not influence the bubble or droplet shape or the subsequent structure. This, along with the previously discussed static assumption, results in the absence of a capillary number dependence in this model. However, the fluid property that will influence the shape the most is the interfacial tension, which will affect the curvature of the interface as the bubble or drop conforms to the rectangular corners of the channel.[23,24] Since a change in curvatures along the corners of the bubble amounts to a shape change, this variation will also contribute to uncertainty in the measured volume.

The presence of a high concentration of surfactant above the critical micelle concentration ensures monodisperse bubbles and droplets that are stable against coalescence in the microchannel, which meets several key criteria of the model. We consider only small molecule surface active species in this study, which can easily adsorb and desorb at the interface to allow the bubble or droplet shape to relax to a circular interface.[30,31] We do not consider more complex adsorbing species, such as proteins and particles that may not allow the shape to fully relax.[32]

We also do not address structures formed by polydisperse foams and emulsions even though these can be produced at some conditions in microfluidic nozzles. For example, Raven et al.[7] described production of a bidisperse foam structure, and Garstecki et al.[33,34] reported on oscillations and instabilities associated with bubble formation at certain experimental flow conditions. While we observe these phenomena, the analysis of such cases is outside the scope of this paper. In some cases, very small satellite droplets are formed. These are neglected assuming that they do not significantly affect the calculated bubble volumes and volume fractions.[35,36]

In microfluidic bubble and droplet generation, each type of nozzle operates using a different mode of break-up: flow-focusing and co-flow devices use the elongation of the dispersed phase stream to induce break-up,[12,37] while droplets are formed by shear flow in T-junctions.[38,39] The different modes of break-up lead to different ranges of accessible bubble volumes and volume fractions as shown in the regime maps of Figs. 6–8. The flow-focusing devices produce smaller bubble volumes for a given volume fraction (see $0.02 \leq \phi_d \leq 0.2$ for Fig. 6 or $\phi_d \sim 0.2$ for Fig. 7) and larger volume fractions for a given bubble volume ($0.1 \leq V^* \leq 1$ for Fig. 6 and $0.01 \leq V^* \leq 1$ for Fig. 7) compared with co-flow devices. A similar comparison is made between flow-focusing devices and T-junction devices ($0.07 \leq \phi_d \leq 0.2$ for a set volume and $0.1 \leq V^* \leq 5$ for a fixed volume fraction) in Fig. 8. Co-flow and T-junction nozzles generate similar sized bubbles and droplets, but T-junctions are able to generate structures with lower volume fractions. However, varying the nozzle type still could not produce experimental data for all of the regimes predicted by the geometric model. Experiments at conditions expected to yield spherical packed foam and bamboo foam structures resulted in either no break-up of the dispersed phase flow or the formation of large bubbles or droplets rather than increased numbers of smaller bubbles or droplets. This can be attributed to the larger mechanical stresses needed to overcome large Laplace pressures inside smaller bubbles.[40] At the high speeds needed to achieve larger mechanical stresses, there is also less time for surfactants to adsorb to and stabilize the interface, so the interfacial tension is larger and the break-up of the dispersed phase into smaller droplets is less likely.[25]

Finally, we have already considered the limit of the geometric model that occurs when the depth and width of the channel are equal (Fig. 8). At the other extreme, we can consider an infinitely wide channel ($\Lambda \to 0$). In direct contrast to the case of $\Lambda = 1$, in which the pancake regime collapses, the pancake region in this case will have no upper bound and the slug and bamboo foam regions will effectively disappear. In this limiting case, the structure cannot become packed for either sphere or pancake shapes because there is no maximum number of rows, so the packed foam regions will also disappear when $\Lambda \to 0$. In summary, an infinitely wide channel will yield only spheres and pancakes in dripping and alternating structures, and the critical dimensionless volume defining the transition between shapes will approach $V^* \to 0$ as $\Lambda \to 0$.

We have outlined some limitations and key criteria for the present model and experimental setup and we observe that a single microfluidic nozzle design cannot access certain regions of the operating diagram, specifically the packed and bamboo foam regions. However, future modifications to the experimental setup can be considered to access these regimes. For example, a method by which continuous fluid can be removed would allow the dispersed phase volume fraction to increase within the outlet channel. This can be accomplished by including an additional side channel.[41] Alternatively, the foam or emulsion could be compressed such that the effective length of the channel decreases by forcing the excess liquid out of the channel and causing the inclusions to deform and rearrange as necessary.[19] The bubble or droplet volume can also be controlled by the introduction of an automated system that would allow for a greater accessible range of bubble and droplet sizes, such as one that incorporates external valves.[42]

VI. CONCLUSIONS

We have developed a geometric model for the shape and structure of a foam or emulsion confined within a rectangular microchannel. The critical volumes and volume fractions at which the transitions between bubble shapes (sphere, pancake, or slug) and structures (dripping, slug, alternating foam, packed foam, or bamboo foam) occur are described and used to generate operating diagrams for three downstream microchannel aspect ratios. Experiments agree reasonably well with the geometric model indicating that the underlying simplifying assumptions are valid over a relatively wide range of conditions. Bubble and droplet data from flow-focusing, T-junction, and co-flow devices were used to compare the geometric model with experimental results. The most significant shortfall of the geometric arguments is the lack of accounting for flow effects. Flow effects most strongly influence the highly confined shapes and highly packed structures, and the effect is that the boundaries between regimes are blurred. These results, particularly the predicted transition conditions outline in Eq. (18) through Eq. (22), lead to a set of design criteria that can be used as a starting point for generating desired foam or emulsion structures for many applications.

ACKNOWLEDGMENTS

[1] K.-Y. Chung, N. C. Mishra, C.-C. Wang, F.-H. Lin, and K.-H. Lin, Biomicrofluidics **3**, 022403 (2009).
[2] M. Devaud, T. Hocquet, and V. Leroy, Eur. Phys. J. E **32**, 13 (2010).
[3] A. C. Hatch, J. S. Fisher, S. L. Pentoney, D. L. Yang, and A. P. Lee, Lab Chip **11**, 2509 (2011).
[4] G. M. Whitesides and A. D. Stroock, Phys. Today **54**, 42 (2001).
[5] A. M. Gañán-Calvo and J. M. Gordillo, Phys. Rev. Lett. **87**, 274501 (2001).
[6] G. F. Christopher and S. L. Anna, J. Phys. D **40**, R319 (2007).
[7] J. P. Raven, P. Marmottant, and F. Graner, Eur. Phys. J. B **51**, 137 (2006).
[8] D. Weaire, S. Hutzler, W. Drenckhan, A. Saugey, and S. Cox, "Rheology of foams," in *Progress in Colloid and Polymer Science: Smart Colloidal Materials*, edited by W. Richtering (Springer, Berlin/Heidelberg, 2006), Vol. 133, pp. 100.
[9] J. I. Park, E. Tumarkin, and E. Kumacheva, Macromol. Rapid Commun. **31**, 222 (2010).
[10] A. S. Utada, E. Lorenceau, D. R. Link, P. D. Kaplan, H. A. Stone, and D. A. Weitz, Science **308**, 537 (2005).
[11] B. P. Binks and T. S. Horozov, *Colloidal Particles at Liquid Interfaces* (Cambridge University Press, Cambridge, England, 2006).

[12]P. Garstecki, I. Gitlin, W. Diluzio, G. M. Whitesides, E. Kumacheva, and H. A. Stone, Appl. Phys. Lett. **85**, 2649 (2004).

[13]E. B. Matzke, Am. J. Bot. **33**, 58 (1946).

[14]W. Drenckhan and D. Langevin, Curr. Opin. Colloid Interface Sci. **15**, 341 (2010).

[15]W. L. Olbricht, Annu. Rev. Fluid Mech. **28**, 187 (1996).

[16]E. Kumacheva, P. Garstecki, H. K. Wu, and G. M. Whitesides, Phys. Rev. Lett. **91**, 128301 (2003).

[17]S. Yang, S. Ahn, A. Kang, D. Lee, S. Lee, J. Kim, K. Ahn, and S. Lee, Korea-Aust. Rheol. J. **23**, 119 (2011).

[18]P. Pieranski, L. Strzelecki, and B. Pansu, Phys. Rev. Lett. **50**, 900 (1983).

[19]J.-B. Fleury, O. Claussen, S. Herminghaus, M. Brinkmann, and R. Seemann, Appl. Phys. Lett. **99**, 244104 (2011).

[20]P. Garstecki and G. M. Whitesides, Phys. Rev. E **73**, 031603 (2006).

[21]P. Garstecki and G. M. Whitesides, Phys. Rev. Lett. **97**, 024503 (2006).

[22]See supplementary material at http://dx.doi.org/10.1063/1.3693605 for a more detailed description of the geometric model for the foam structure.

[23]H. Wong, C. J. Radke, and S. Morris, J. Fluid Mech. **292**, 71 (1995).

[24]H. Wong, C. J. Radke, and S. Morris, J. Fluid Mech. **292**, 95 (1995).

[25]W. Lee, L. M. Walker, and S. L. Anna, Phys. Fluids **21**, 032103 (2009).

[26]T. Cubaud and C. M. Ho, Phys. Fluids **16**, 4575 (2004).

[27]M. J. Fuerstman, A. Lai, M. E. Thurlow, S. S. Shevkoplyas, H. A. Stone, and G. M. Whitesides, Lab Chip **7**, 1479 (2007).

[28]A. Nadim and H. A. Stone, Stud. Appl. Math. **85**, 53 (1991).

[29]D. Weaire and S. Hutzler, *The Physics of Foams* (Oxford University Press, New York, 2001).

[30]J. Eastoe and J. S. Dalton, Adv. Colloid Interface Sci. **85**, 103 (2000).

[31]R. Pan, J. Green, and C. Maldarelli, J. Colloid Interface Sci. **205**, 213 (1998).

[32]M. Abkarian, A. B. Subramaniam, S.-H. Kim, R. J. Larsen, S.-M. Yang, and H. A. Stone, Phys. Rev. Lett. **99**, 188301 (2007).

[33]P. Garstecki, M. J. Fuerstman, and G. M. Whitesides, Nat. Phys. **1**, 168 (2005).

[34]P. Garstecki, M. J. Fuerstman, and G. M. Whitesides, Phys. Rev. Lett. **94**, 234502 (2005).

[35]S. L. Anna, N. Bontoux, and H. A. Stone, Appl. Phys. Lett. **82**, 364 (2003).

[36]Y.-C. Tan, V. Cristini, and A. P. Lee, Sens. Actuators B **114**, 350 (2006).

[37]R. Q. Xiong, M. Bai, and J. N. Chung, J. Micromech. Microeng. **17**, 1002 (2007).

[38]P. Garstecki, M. J. Fuerstman, H. A. Stone, and G. M. Whitesides, Lab Chip **6**, 437 (2006).

[39]T. Thorsen, R. W. Roberts, F. H. Arnold, and S. R. Quake, Phys. Rev. Lett. **86**, 4163 (2001).

[40]P. C. Hiemenz and R. Rajagopalan, *Principles of Colloid and Surface Chemistry*, 3rd ed. (Marcel Dekker, New York, 1997).

[41]K. Jiang, C. Xue, C. Arya, C. Shao, E. O. George, D. L. Devoe, and S. R. Raghavan, Small **7**, 2470 (2011).

[42]J. Guzowski, P. M. Korczyk, S. Jakiela, and P. Garstecki, Lab Chip **11**, 3593 (2011).

[43]M. Hashimoto, P. Garstecki, and G. M. Whitesides, Small **3**, 1792 (2007).